PIER M

Design of a 3D Printed Wide Band Metasurface Antenna for High Power Applications

Mohamed Z. M. Hamdalla[1,*], Mashrur Zawad[1,2], Matthew Kunkle[1], Somen Baidya[2], Roy C. Allen[1], Peter J. Bland[1], Travis D. Fields[1], and Ahmed M. Hassan[1,2]

[1]*Missouri Institute for Defense & Energy, University of Missouri-Kansas City, Kansas City, MO, USA*
[2]*Department of Computer Science and Electrical Engineering, University of Missouri-Kansas City, Kansas City, MO 64110, USA*

ABSTRACT: Weight-size optimization is the main challenge of high-power antenna design. This paper presents a low-profile, metasurface-based wideband antenna. The proposed antenna comprises an N-type-to-waveguide transition to excite the metasurfaces and handle high-power excitations. A metasurface array of 4×4-unit cells is integrated into the waveguide. The proposed waveguide is 3D printed, and its internal faces are covered by copper tape to maintain a low weight (less than 200 g). The prototype is experimentally tested, and the results confirm the prototype's functionality from 2.1 GHz to 3.6 GHz with a bandwidth of 52.6% and a peak gain of 8.5 dBi. Furthermore, the high-power handling capability of the proposed design has been experimentally confirmed by exciting it with a 7 kV pulsed source. These results demonstrate the applicability of the proposed antenna in radar applications and wireless communication between Unmanned Aerial Vehicles (UAVs).

1. INTRODUCTION

High power antenna design is critical to modern communication systems, in both civilian and defense industries [1–8]. However, the design of high-power antennas poses unique challenges, such as achieving a low profile and wide bandwidth while maintaining a stable gain. Hence, careful consideration must be given to the antenna's ability to handle high power while maintaining the desired performance characteristics [8]. Several high power antennas were reported in recent studies where the main focus has been on the antenna performance at the expense of size, weight, and bandwidth [1, 9, 10, 11]. For example, Guo et al. presented a high-power phased array antenna that operated at 9.6 GHz with a 33 dBi gain [1]. However, its largest dimension was 57λ. Zhao et al. introduced a 31.25λ large all-metal beam steering lens high-power antenna with a narrow bandwidth of 2.13% [9]. The significant form factor in the previously reported studies limits their application to mobile applications such as Unmanned Aerial Vehicles (UAVs). Likewise, in [10, 11], the authors presented high-power reflectarray and conical ground helical antennas, with a 23.4 dBi and 11 dBi gain, respectively. However, their respective bandwidths were 25% and 23.5%, and their respective largest dimensions were 5.38λ and 2.31λ. In this work, we propose using metasurfaces to achieve a novel low-profile antenna with a wideband response.

Recently, metasurfaces have been employed in several novel antenna designs for bandwidth and gain enhancement [12–28]. These enhancements are directly related to improving the design's physical properties, i.e., reducing surface waves and back radiations. Moreover, metasurfaces with negative refractive index properties are utilized as flat lenses, increasing the antenna's directivity and gain by focusing the radiated waves. However, to our knowledge, no studies have specifically established the feasibility of multilayer 2D-metasurface-based high-power antennas. On the other hand, several 3D gradient index (GRIN) metamaterial lenses were introduced for high-power antenna applications [29, 30]. In addition, recently, there has been a rising interest in metamaterial-based high-power sources [31–34].

In this study, we propose a 3D-printed lightweight metasurface-based antenna. An N-type-to-waveguide transition through a thick monopole is designed to excite the metasurfaces with high-power levels. The gain and bandwidth of the design are improved by incorporating a metasurface lens. With this performance, the proposed antenna design is expected to be suitable for high-power mobile radar. A preliminary version of this work was presented in [35].

The novelty of this work is using 3D printing capability to fabricate an N-type-to-waveguide transition suitable for high power applications while maintaining low weight and size compared to recent designs [36, 37]. Another contribution is that unlike most reported studies, which used metasurfaces to serve one purpose, such as increasing antenna gain [38], we introduced it for two completely different purposes. First, it allows the N-type-to-waveguide transition to radiate at lower frequencies efficiently, and second, it further enhances the design's gain. A third contribution is that this work investigates using the multipaction phenomenon for the first time in evaluating antennas' high-power performance.

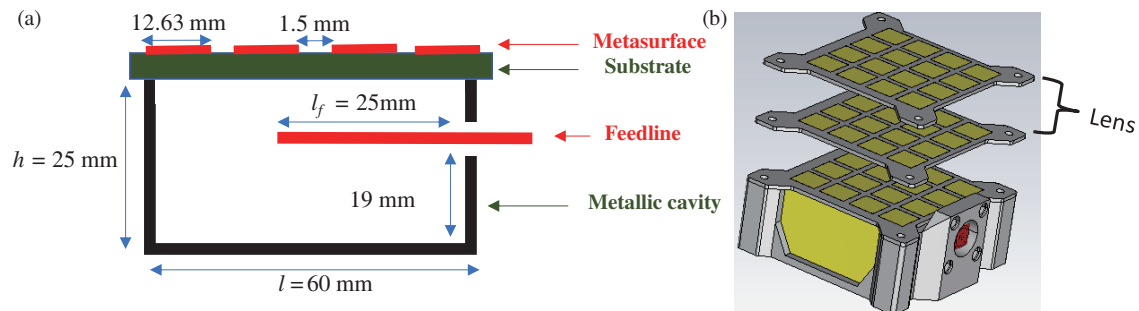* Corresponding author: Mohamed Z. M. Hamdalla (mhamdalla@mail.umkc.edu).

115

FIGURE 1. (a) A sketch of the side view of the metallic cavity design and its dimensions. (b) View of the CST 3D model of the metasurface layer backed with a metallic cavity with lens.
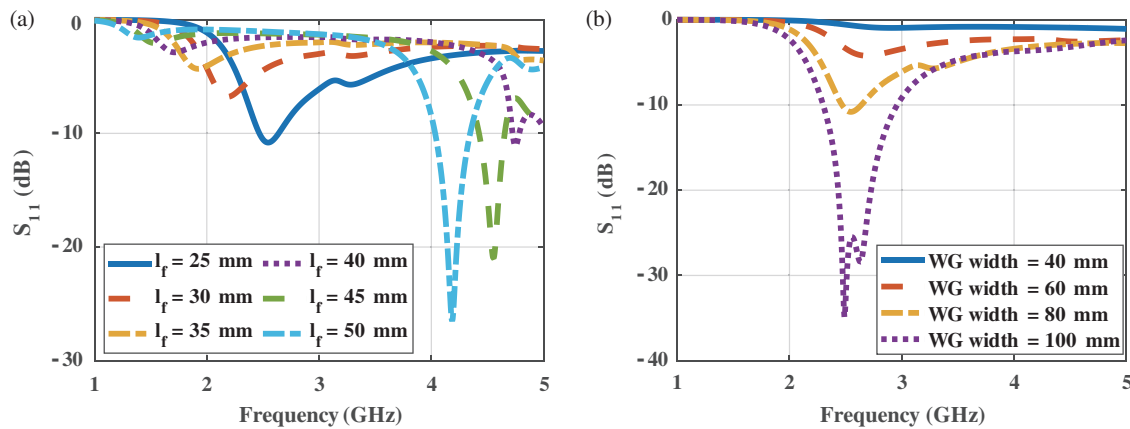

FIGURE 2. Scattering parameters of the N-type-to-waveguide transition dimensions (a) when the waveguide width is fixed to 80 mm and the feedline length is varied, (b) when the feedline length is fixed to 25 mm and the waveguide width is changed.

2. CONFIGURATION, DESIGN, AND SIMULATION

The antenna design process consists of two sequential steps. The first step involves designing the N-type-to-waveguide transition at a desired frequency range. The subsequent step involves incorporating metasurface lenses to enhance the overall antenna performance in terms of gain and bandwidth. The antenna is designed, and its performance is verified using CST Studio Suite full-wave time domain solver [39]. A schematic view of the proposed metasurface antenna design is depicted in Fig. 1. The monopole is set at the center of the front face of the waveguide, away from its walls, to avoid high power discharges. Therefore, the proposed design's power handling capability is limited by the power handling capability of its N-type connector and the air breakdown. The rectangular waveguide (WG) dimensions are $60\,\text{mm} \times 60\,\text{mm} \times 25\,\text{mm}$. The size of the waveguide is designed to support frequencies $< 3\,\text{GHz}$. For air filled and TE_{10} mode operation, the resonance frequency is calculated according to Equation (1) [40]:

$$f_c = \frac{c}{2w_g} \qquad (1)$$

where f_c is the cutoff frequency of the waveguide, c the speed of light, and w_g the WG width. The selection of the WG dimensions and the monopole are critical for defining the resonance frequency of the N-type-to-waveguide transition.

A parametric study is conducted to check the contribution of each element of the N-type-to-waveguide transition, i.e., the WG length and feedline length and location. The parametric study is conducted only for the metallic cavity before incorporating the metasurface layer. Fig. 2(a) illustrates that when the feedline length is 25 mm and WG width is 80 mm, it resonates efficiently at $\sim 2.5\,\text{GHz}$. However, if the WG width decreases beyond 80 mm, the WG cannot support this frequency; hence the resonance starts to vanish as shown in Fig. 2(b). Contrarily, the feedline's resonance strongly resonates when the cavity width increases to 100 mm. However, the proposed next step involves changing the WG behavior by incorporating metasurface to improve the model's matching. Therefore, we fix the feed length to 25 mm and the WG width to 60 mm. The short feedline length is chosen to maintain a big separation between its tip and the cavity wall to avoid arcing at low power as will be illustrated later. In addition, the separation between the feedline and the bottom of the cavity is optimized through the parametric study to maintain the response shown in Fig. 2.

The N-type-waveguide transition model is then used to feed the metasurface layer electromagnetically, with no electrical connection, as shown in Fig. 1(a). The N-type-waveguide transition integrated with the metasurface will be referred to as a "cavity" in the rest of this study. Fig. 1(b) shows the CST 3D model of the cavity model along with the model of the cavity when it is improved by adding extra lenses. The metasurface
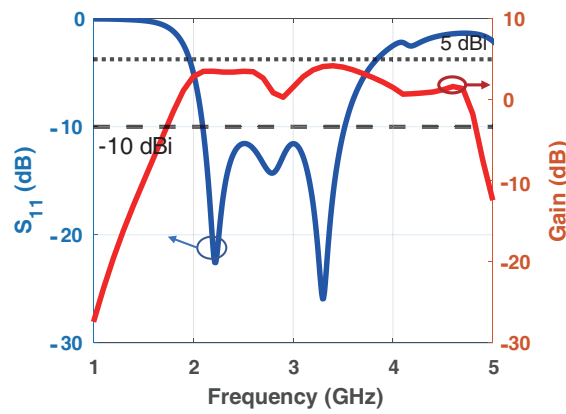
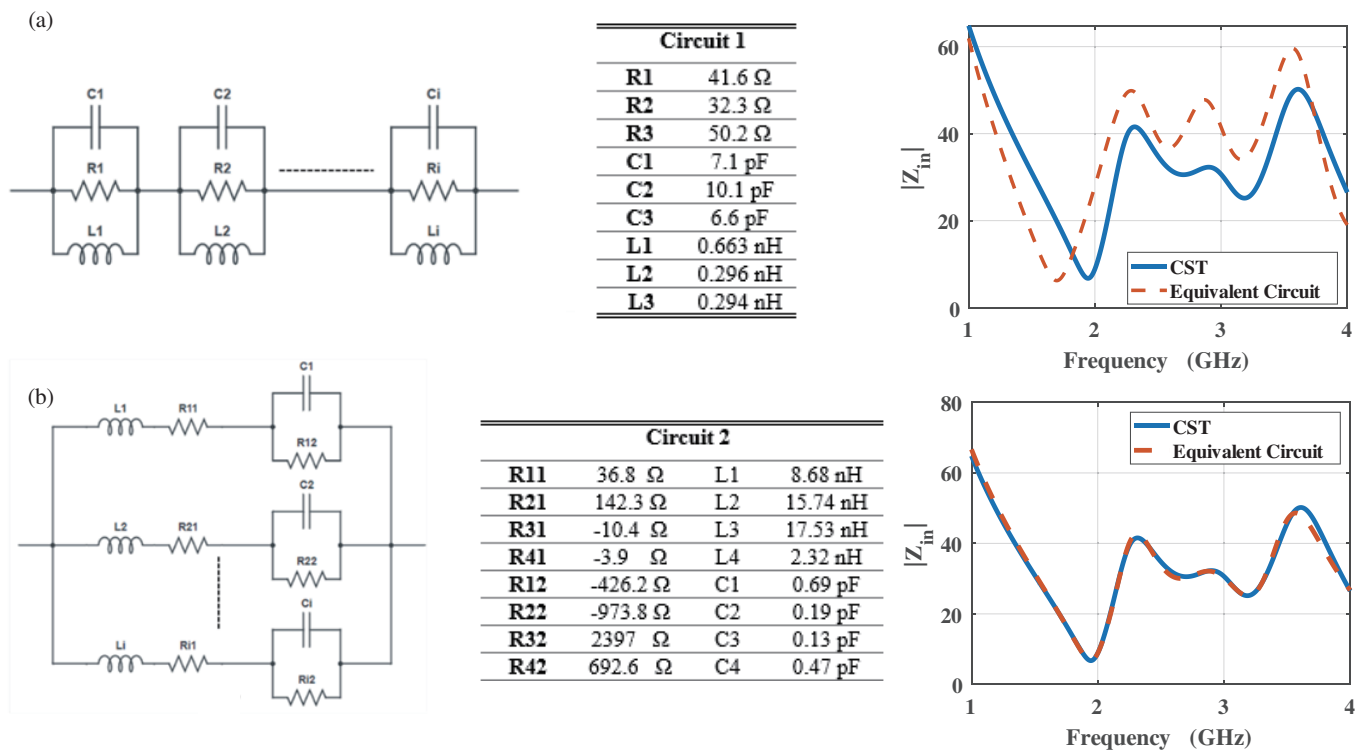**FIGURE 3**. The scattering parameters and the realized gain of the cavity.

FIGURE 4. Circuit representation of the antenna input impedance and its comparison with CST. (a) Circuit 1 representation. (b) Circuit 2 representation.

layer consists of 4×4 square metallic patches, each with an edge length of 12.63 mm and separated by 1.5 mm. The array of patches is designed above a 1.6 mm FR-4 substrate with relative permittivity $\varepsilon_r = 4.3$. The low permittivity substrate helps achieve high bandwidth while maintaining a compact size [41]. The initial dimensions and the number of patches are chosen based on the design proposed in [41]. Then, a parametric study was conducted to optimize the patches' physical parameters to achieve the optimum bandwidth and gain.

Figure 3 illustrates the cavity antenna's scattering parameters and gain. It demonstrates that the design has a 52.6% bandwidth and 5 dBi gain throughout the frequency range. Comparing Fig. 3 with Fig. 2 clearly indicates the metasurface layer's contribution to improving the cavity antenna's bandwidth.

In addition, the equivalent circuit model of the proposed antenna is estimated. The two different circuit topologies reported in [42] are adopted in this study. The two representations are categorized as (*i*) Circuit1: In this circuit representation, each resonance in the input impedance is represented by a parallel RLC branch as shown in Fig. 4(a), and (*ii*) Circuit 2: In this circuit representation, the input impedance is modeled as a summation of N arbitrarily weighted poles. Poles typically exist in conjugate pairs. Each pair can be represented by a Second Series-Equivalent-Circuit branch consisting of an inductor, a capacitor, and two resistors, connected as shown in Fig. 4(b). The detailed calculation of the value of each component is presented in [42]. It is important to note that despite the accuracy of the Circuit 2 topology, it is almost impossible to implement this
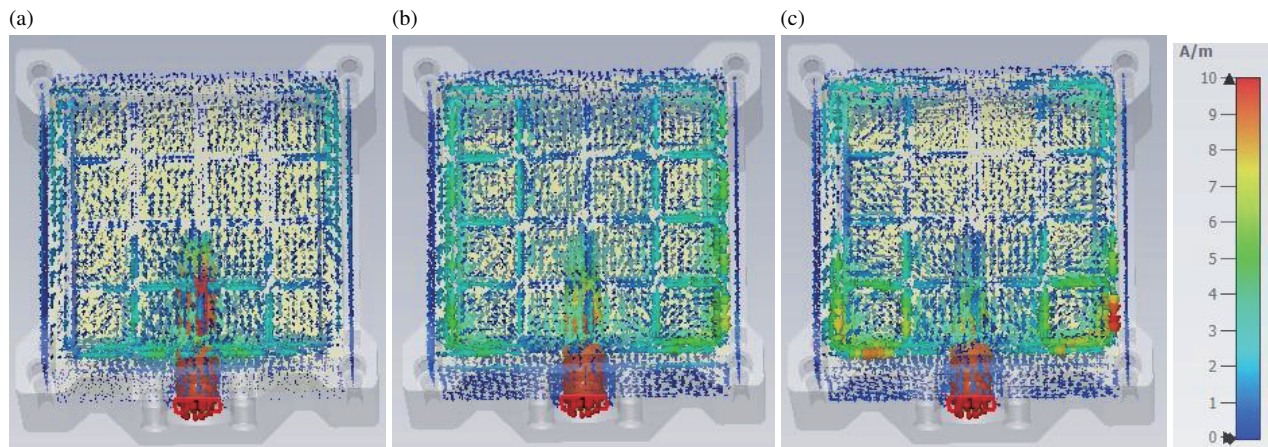
FIGURE 5. The current distribution of the proposed antenna at (a) 2.4 GHz, (b) 2.8 GHz, and (c) 3.4 GHz.

circuit because of the negative resistor values resulting from this topology [42]. The corresponding response of each circuit topology is shown in Fig. 4. Clearly, circuit 2 topology provides the best matching.

Moreover, Fig. 5 shows the proposed model's surface current distribution. The current is mainly distributed across the feedline, and the currents on the metasurface layer are less because there is no physical contact between it and the feedline.

Furthermore, the antenna fidelity factor (FF) is evaluated to verify the robustness of the proposed design's signal integrity. The FF depicts the antenna's capability to transmit and receive signals without distorting the temporal profile of the signal [43]. The FF of an antenna can be mathematically represented as the cross-correlation between the transmitted and received signals in the time domain as follows [43] :

$$FF = max_t \frac{\int_{-\infty}^{\infty} T_s(t) R_s(t+\tau) dt}{[\int_{-\infty}^{\infty} |T_s(t)|^2 dt]^{1/2} [\int_{-\infty}^{\infty} |R_s(t)|^2 dt]^{1/2}} \quad (2)$$

where $T_s(t)$ is the transmitted signal, $R_s(t)$ the received signal, and τ the time delay between the two signals. FF of 1 indicates that the received signal retains the exact shape and characteristics of the transmitted signal, signifying excellent signal integrity. On the other hand, if the FF is less than 0.5, it indicates significant distortion in the received signal, suggesting a substantial deviation from the original transmitted signal.

The proposed antenna's FF is estimated for face-to-face orientation, as shown in Fig. 6(a). Hence, one antenna will transmit while the other identical one will receive the signal. The distance between the transmitter and receiver antennas is 500 mm. CST microwave studio calculates the received signal at one antenna when the other is excited by the default CST Gaussian pulse covering the entire frequency range (2.1–3.6 GHz). The excitation and received signal are then used to calculate the FF in Eq. (2), and the FF of the antenna is 0.943. The comparison of normalized amplitudes of the input and output signals is shown in Fig. 6(b). The FF results emphasize the proposed antenna's excellent performance in maintaining the transmitted signals' fidelity.

In addition, the System Fidelity Factor (SFF), which calculates the distortion produced by an antenna when transmitting a pulse to another antenna [44] is also evaluated for the prototype at different angles. To estimate the angular SFF, the receiving antenna is rotated around the access of the transmitting antenna with a 10° step. The reference angle is that when the antennas are in face-to-face configuration as shown in Fig. 6(a). The SFF is demonstrated in Fig. 6(c), which indicates the proposed antenna's ability to radiate at all angles without distorting the radiated signal. That is, the minimum achievable SFF is 0.689, while the maximum value is 9.43.

Moreover, the group delay, which measures the absolute signal delay and the phase distortion between the input and antenna output [44] is calculated for the face-to-face configuration and shown in Fig. 6(d). The small peak-to-peak group delay, less than 1 ns and the near-constant with very few ripple responses indicate the minimum signal distortion across the band. The result of the group delay agrees with the expected behavior from the SFF for the same configuration.

To further improve the gain of the proposed antenna, we incorporated a 2-layer metasurface lens over the antenna, as illustrated in Fig. 1(b). The lens analysis was carried out for one layer, and the second layer was added to further improve the lens' gain. We carried out a comparative analysis of the scattering parameters and gain of the antenna with the lens incorporation. The lens is 22.5 mm from the metasurface antenna, corresponding to $\sim \lambda/4$ of the center frequency, and has the same design and substrate material as the metasurface layer.

Figure 7 compares the S-parameters and the antenna gain with and without the lens when using FR-4 as the substrate for both the metasurface layer and lenses. The antenna gain increased from 5 dBi to 8.5 dBi, indicating a gain improvement of ~ 3.5 dBi after adding the lens, as illustrated in Fig. 7(b). Notably, the gain increased with the operation band of the antenna (2.1–3.6 GHz) and worsened due to the high reflection outside the band. In addition, the FF of the antenna after incorporating the lens is recalculated, and its value is 0.963.
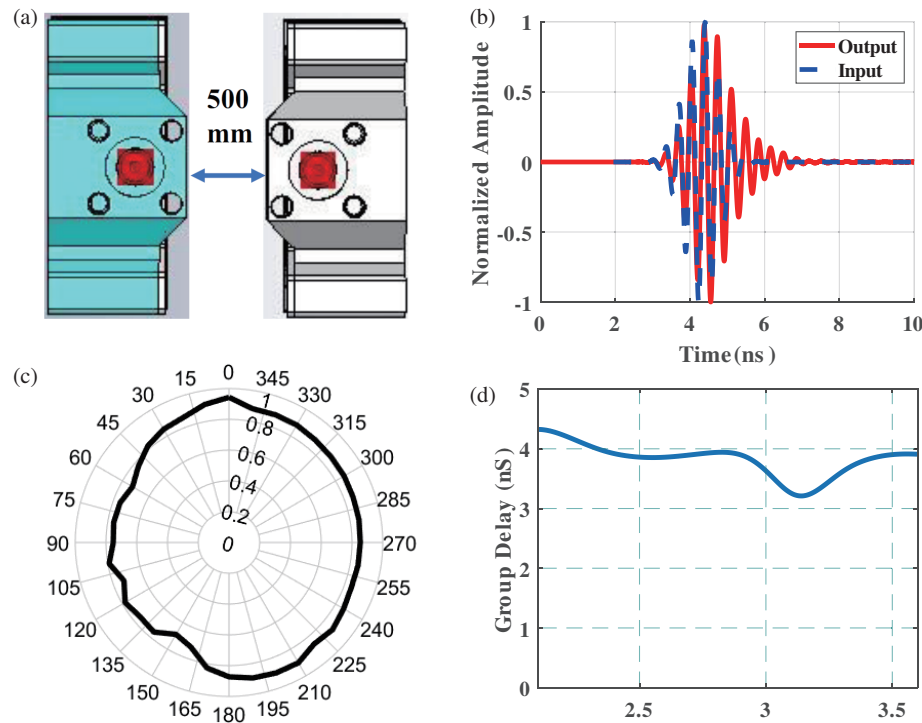
FIGURE 6. (a) Photograph of the configuration used to test the fidelity factor. (b) Time vs. normalized amplitude of the input and output signal for the face-toface having. (c) The angular SFF of the proposed antenna. (d) The group delay of the proposed antenna.
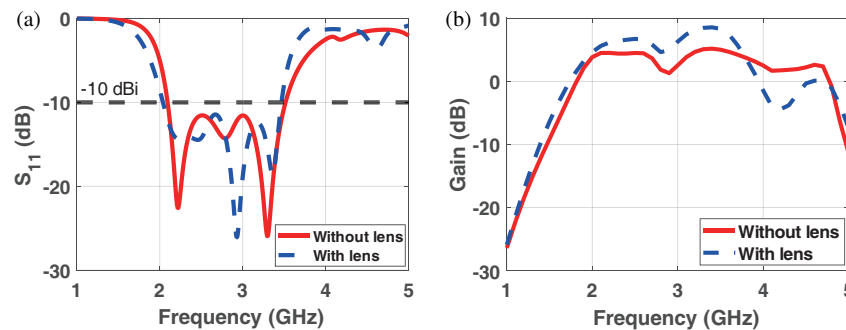

FIGURE 7. The Scattering parameters, (b) the realized gain of the cavity design with and without the lens.

In addition, Figs. 8 and 9 illustrate the proposed antenna's 2D and 3D far-field patterns, receptively indicating the maximum gain of 8.5 dBi for the antenna with the lens.

Moreover, Fig. 10 illustrates the radiation efficiency of the proposed antenna with and without the lens. The results demonstrate the high efficiency achieved by the proposed model.

As illustrated in the previous section, the proposed model is suitable for high power applications. Hence, the RF breakdown of the proposed design needs to be evaluated. For such analysis, we propose, for the first time, using a multipactor and ionization breakdown evaluation [45]. Multipactor is a physical phenomenon resulting in air breakdown caused by the electron resonance effect. When the high-intensity EM fields accelerate primary electrons, the electron collides on the device walls. It generates secondary electrons, leading to an uncontrolled electron discharge and a breakdown in the air inside the waveguide [45].

We used the CST studio suite Spark3D tool to analyze the proposed structure for multipactor simulation. The antenna's EM fields were extracted at the resonance frequency (2.85 GHz). The general workflow of the CST Multipactor analysis can be summarized as follows:

- Perform EM analysis of the antenna structure while requesting 3D E, H, and far field at the design's resonant frequency.

- Export 3D EM fields to the Spark3D interface and define the analysis region.

- Progressively increase the power level while monitoring the electron evolution until the breakdown is achieved.

- Locate discharge build-up and discharge locations by analyzing the results.
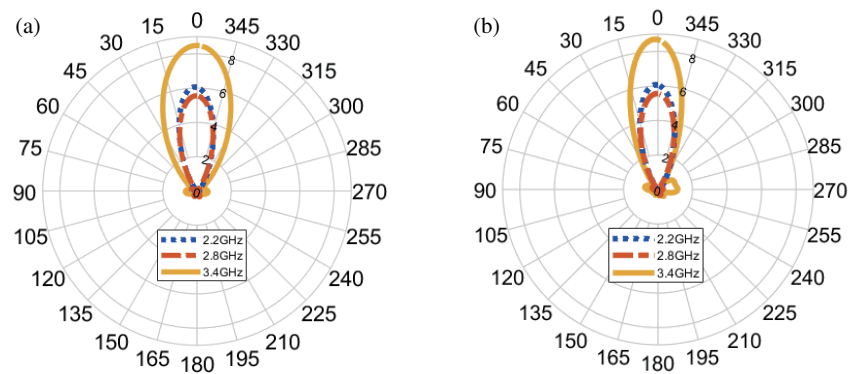
FIGURE 8. The radiation pattern at three different frequencies for the proposed antenna at three different frequencies. (a) Without lens. (b) With lens.
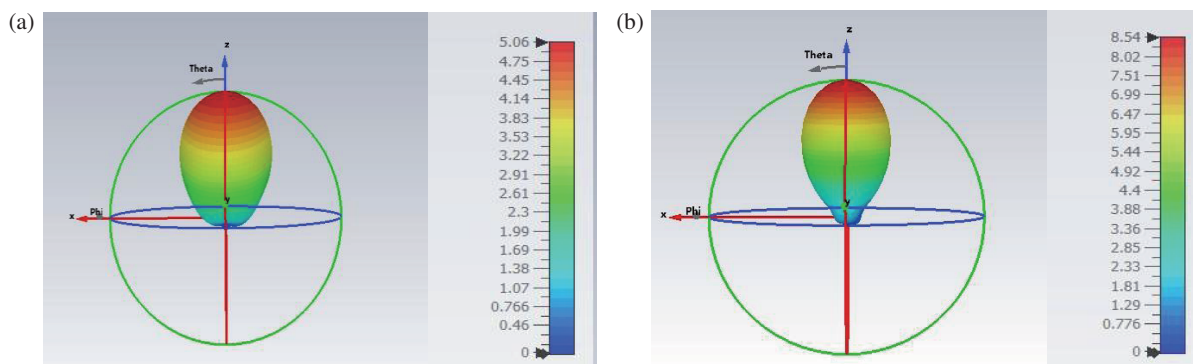

FIGURE 9. 3D radiation pattern of the proposed antenna at 3.4 GHz. (a) Without the lens. (b) With the lens.
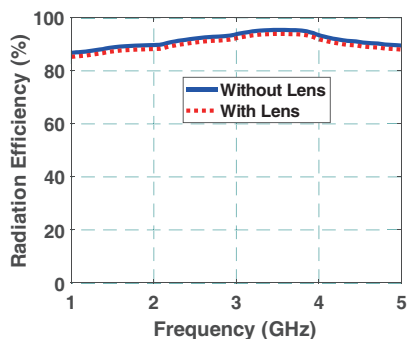

FIGURE 10. Radiation efficiency of the proposed antenna with and without the lens.

The curves in Fig. 11(a) represent the electron evolution with time for each power analyzed. The legends in Fig. 11(a) indicate whether each analyzed power has achieved a breakdown. When a breakdown occurs for a certain input power, the multipactor order is given, whereas when there is no breakdown, the message "No break" appears. As the secondary electron dies out at a specific power, there is no multipactor or air breakdown at those power levels, whereas beyond a certain power, the electron evolution leads to a breakdown of a specific order. Based on the analysis, the solver progressively increases the input power level while monitoring the electron evolution until

breakdown is achieved. Fig. 11(a) indicates that the proposed antenna's breakdown power is 2.05 MW for 40 ns excitation.

Moreover, we can also analyze the discharge location from the 3D structure view at a given power level. We used 3 MW power for this specific analysis, which is just above the maximum allowable power limit from our multipactor analysis. As shown in Fig. 11(b), the avalanche breakdown occurs at the tip of the monopole, where the E field strength is maximum. The red dots in Fig. 11(b) represent the accumulation of Charges at 20 ns, leading to a spark inside the air region of the cavity. The breakdown occurred between the monopole and metasurface layer due to the small relative separation between them compared to the other walls of the cavity. One advantage of the multipactor analysis is determining the cause of the breakdown. Hence, it allows further improvement of the design. For instance, in this design, if the size is not a limitation of the application, increasing the height of the cavity would be a solution to push the limits of the high-power capability. In addition, adding a layer of dielectric or gases such as SF6 inside the cavity would also improve the power handling capability. The results provided in this section ensure the applicability of the proposed design for high power mobile applications.

3. MEASUREMENT AND RESULT

The proposed N-type-waveguide transition is 3D printed out of PLA. 0.03 mm copper tapes are then added to cover the internal
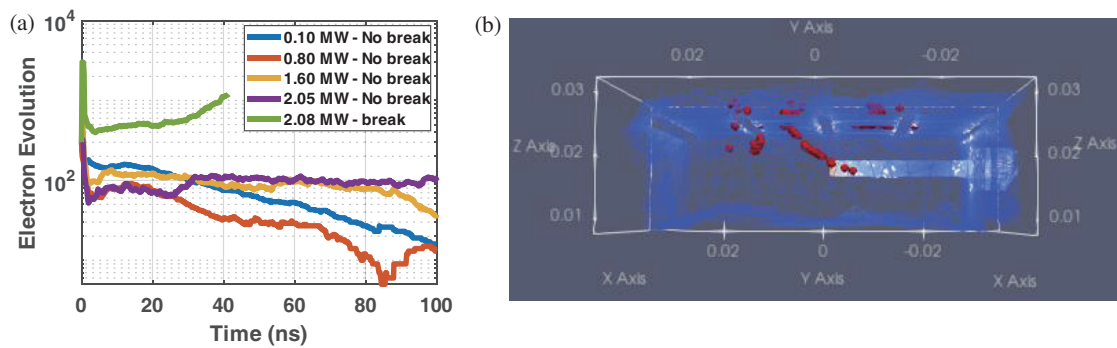
FIGURE 11. (a) The Multipactor results of the cavity-backed design without lens. (b) A photograph of the electron discharge at the cavity breakdown backed design without the lens.
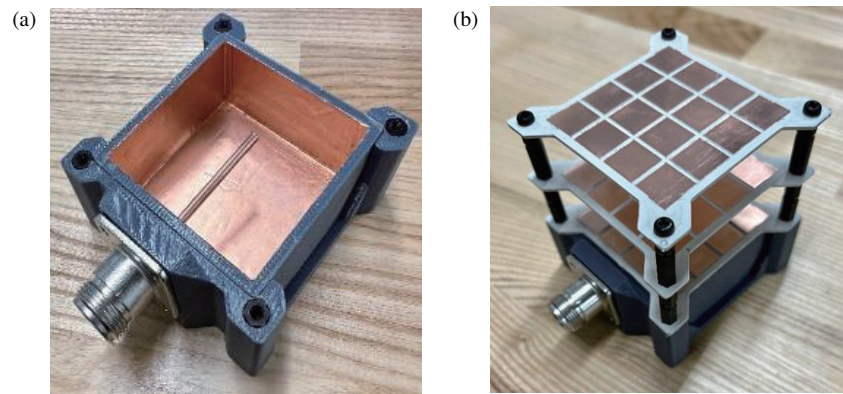

FIGURE 12. (a) A photograph of the fabricated model of the cavity and the monopole feed, (b) a photograph of the fabricated metasurface antenna with the lens.
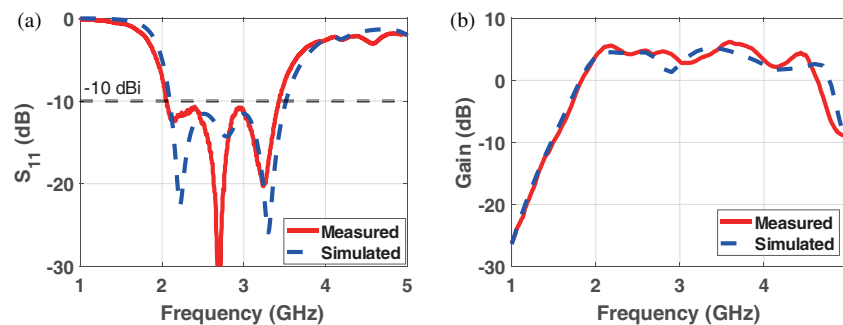

FIGURE 13. Comparison of simulated and measured parameters of the prototype without lens. (a) S-parameters and (b) gain characteristics.

walls of the plastic prototype. The 3D printed prototype with copper tapes gives the low-weight advantage over a complete metallic design. The overall prototype weighs less than 200 g. The metasurface layer and 2-layer metasurface lens are fabricated with an FR-4 substrate.

Figure 12 (a) shows the fabricated prototype of the N-type waveguide transition. Fig. 12 (b) shows the complete design of the proposed antenna with the metasurface layer and 2-layer metasurface lens.

The S-parameters of the fabricated prototype are measured and compared with the simulation results. A standard dual-ridge horn antenna is used to measure the gain of the fabricated model in a semi-anechoic chamber. Figs. 13(a) and (b) show

the comparison of the measured and simulated S-parameters and the gain of the prototype without the lens. The dashed black lines in Fig. 13(a) indicate the $-10\,\mathrm{dBi}$ reference of the S-parameters. Perfect agreement between the simulated and measured response is achieved. The comparison in Fig. 13 confirms that the proposed design achieved 52.6% bandwidth and 5 dBi gain without the lens.

In addition, Figs. 14(a) and (b) compare the S-parameters and gain when the lens is incorporated into the antenna design. Perfect agreement between the simulated and measured responses is achieved. The measurement results indicated that incorporating the FR-4 lenses improved the gain by $\sim 3.5\,\mathrm{dBi}$.
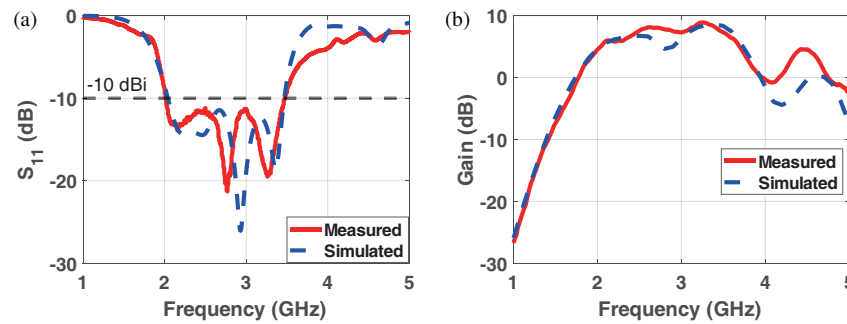
FIGURE 14. Comparison of simulated and measured parameters of the prototype with lens. (a) S-parameters and (b) gain characteristics.
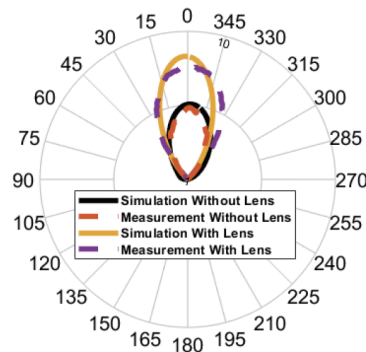

FIGURE 15. Comparison of the prototype's simulated and measured radiation pattern with and without lens.

TABLE 1. Comparison with reported cavity antennas.

Ref.	Center Frequency (GHz)	Bandwidth (%)	Cavity Type	Gain (dBi)	Aperture Size ($\lambda \times \lambda$)
[36]	4	15	Full Metal	12.4-13.4	1.68×1.41
[38]	5.6	20.65	Open Sides	12.3	1.86×1.86
[46]	3.71	6.2	Full Metal	11	1.2×0.7
[47]	25	21.4	Open Sides	15.4	5×4
[48]	9.2	32.7	Open Sides	14.2	4.1×4.1
[49]	3.45	18.6	Full Metal	7.65	0.7×0.7
This Work	2.85	52.6	3D Printed	8.5	0.57×0.57

Moreover, the radiation pattern of the prototype with and without the lens is measured and compared to the simulated results as shown in Fig. 15. Good agreement between the simulated and measured radiation patterns is observed. The radiation pattern indicates almost no back radiation which is a crucial aspect of high-power antennas since the electronics for signal processing are generally housed in the rear part of the antenna, and high field levels can compromise its functioning.

To assess the power handling capability of the proposed design, a high-power test is conducted where the prototype is connected to a high voltage pulsed source ($\sim 7\,\text{kV}$). The 7 kV high-voltage pulsed source is the highest available source at the testing facility, but it does not resample the 2.05 MW source required to reach the breakdown of the proposed antenna. Hence, the 7 kV source is used to confirm the ability of the proposed design to handle high power. D-dots are placed 1 m and 3 m

away from the antenna to measure the power density of the radiated fields, as shown in Fig. 16. The measured power densities of the radiated fields from the prototype at 1 m and 3 m are $115.4\,\text{kW/m}^2$ and $21\,\text{kW/m}^2$, respectively. The experiments were closely monitored, and no sparks were reported. In addition, the S-parameters of the two prototypes, i.e., FR-4 with and without lens, are remeasured after the high voltage test, and the response does not change. That is, no physical damage occurred to the design. Note that the maximum power of our source limits the experimental assessment of the power handling capability of the proposed antenna. However, the simulation results shown in Fig. 11 indicate that the power handling capability of the antenna is much higher at approximately 2.05 MW.

A comparison with a few recently reported cavity antennas is shown in Table 1. The proposed antenna has higher bandwidth
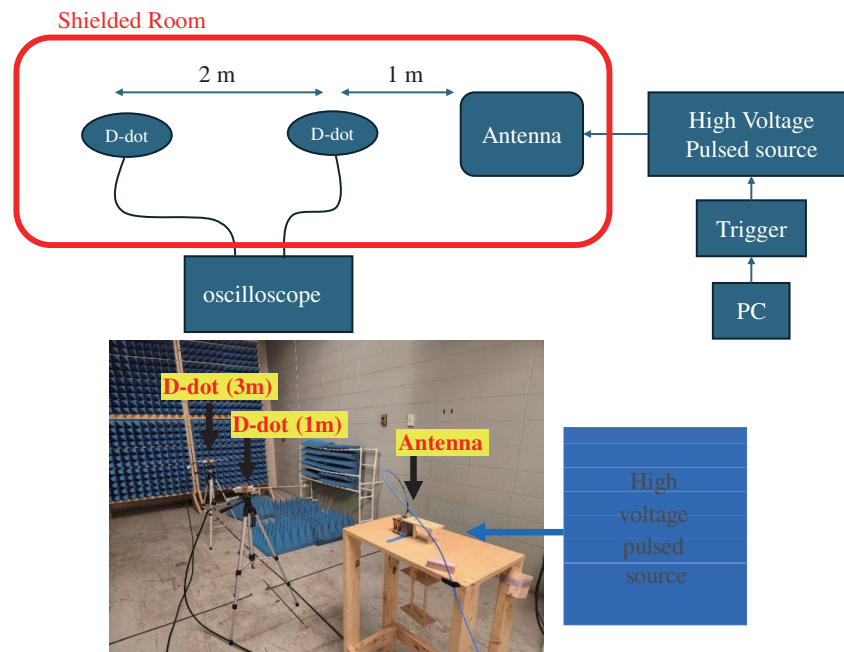
PIER M

FIGURE 16. The measurement setup for the high voltage test. (a) A sketch. (b) A photograph of the actual experimental setup.

but lower gain than [36, 38, 46–48] due to its electrically small size. However, the proposed design is electrically small and has a broader bandwidth than the reported antennas. In addition, the proposed design has a superior performance compared to [49].

4. CONCLUSION

This study presents a novel low-profile wideband antenna for aerial and radar applications. The prototype consists of an N-type-waveguide transition and a metasurface layer. It has a 52.6% and 5-dBi gain. The antenna's gain and directivity are further enhanced by adding a 2-layer metasurface lens on top of the radiating structure. The metasurface lens used in this work consists of 4×4 square patches. The metasurface lenses improved the gain by 3.5 dBi, leading to an overall antenna gain of 8.5 dBi.

Moreover, the antenna achieved a maximum fidelity factor of 0.96 during pulsed transmission and reception. The design is fabricated using a 3D printer, and the internal walls of the cavity are covered with copper taps, leading to a light overall weight. The simulated bandwidth and gain results are verified through experimental measurement with excellent agreement. The power handling capability of the prototype is experimentally tested with a 7 kV source, while the simulation results show that the design can handle up to 2.05 MW. Further optimization of the metasurface patches' shapes, sizes, and distribution will also be performed in the future to increase the gain further while maintaining the overall size of the antenna.

ACKNOWLEDGEMENT

REFERENCES

[1] Guo, L., W. Huang, C. Chang, J. Li, Y. Liu, and R. Meng, "Studies of a leaky-wave phased array antenna for high-power microwave applications," *IEEE Transactions on Plasma Science*, Vol. 44, No. 10, 2366–2375, Oct. 2016.

[2] Samartsev, A., K. A. Avramidis, G. Gantenbein, G. Dammertz, M. Thumm, and J. Jelonnek, "Efficient frequency step-tunable megawatt-class D-band gyrotron," *IEEE Transactions on Electron Devices*, Vol. 62, No. 7, 2327–2332, Jul. 2015.

[3] Song, W., X. Zhang, C. Chen, J. Sun, and Z. Song, "Enhancing frequency-tuning ability of an improved relativistic backward-wave oscillator," *IEEE Transactions on Electron Devices*, Vol. 60, No. 1, 494–497, Jan. 2013.

[4] Fokin, A. P. and A. V. Savilov, "Frequency tuning in the gyrotron oscillator with a klystronlike sectioned cavity," *IEEE Transactions on Electron Devices*, Vol. 62, No. 10, 3393–3398, Oct. 2015.

[5] Wu, P., J. Fan, Y. Teng, Y. Shi, Y. Deng, and J. Sun, "Tunability over three frequency bands induced by mode transition in relativistic backward wave oscillator with strong end reflections," *Physics of Plasmas*, Vol. 21, No. 10, 103110, Oct. 2014.

[6] Xiao, R., C. Chen, W. Tan, and Y. Teng, "Influences of the modulation cavity and extraction cavity on microwave generation and starting oscillation in a klystron-like relativistic backward wave oscillator," *IEEE Transactions on Electron Devices*, Vol. 61, No. 2, 611–616, Feb. 2014.

[7] Ling, J.-P., J.-T. He, J.-D. Zhang, T. Jiang, and L.-L. Song, "A Ku-band coaxial relativistic transit-time oscillator with low guiding magnetic field," *Laser and Particle Beams*, Vol. 32, No. 2, 295–303, 2014.

[8] Kong, G., W. Du, P. Cui, Y. He, and R. Chen, "Design of an electronically beam-scanned high-power capacity reflectarray antenna based on liquid crystals for airborne radar application," in *Proceedings of the 10th Chinese Society of Aeronautics and Astronautics Youth Forum*, 718–724, 2023.

[9] Zhao, X., C. Yuan, L. Liu, S. Peng, Q. Zhang, L. Yu, and Y. Sun, "All-metal beam steering lens antenna for high power microwave applications," *IEEE Transactions on Antennas and Propagation*, Vol. 65, No. 12, 7340–7344, Dec. 2017.

[10] Kong, G., X. Li, Q. Wang, and J. Zhang, "A wideband reconfigurable dual-branch helical reflectarray antenna for high-power microwave applications," *IEEE Transactions on Antennas and Propagation*, Vol. 69, No. 2, 825–833, Feb. 2021.

[11] Cha, S. H., J. S. Choi, J. Ryu, H.-O. Kwon, S.-M. Lee, D.-H. Son, and Y. J. Yoon, "Conical ground helical antenna with feed-through insulator for high-power microwave applications," *Journal of Electromagnetic Engineering and Science*, Vol. 22, No. 5, 537–543, 2022.

[12] Khaleel, S. A., E. K. I. Hamad, N. O. Parchin, and M. B. Saleh, "MTM-inspired graphene-based THz MIMO antenna configurations using characteristic mode analysis for 6G/IoT applications," *Electronics*, Vol. 11, No. 14, 2152, 2022.

[13] Hussain, N., M.-J. Jeong, A. Abbas, T.-J. Kim, and N. Kim, "A metasurface-based low-profile wideband circularly polarized patch antenna for 5G millimeter-wave systems," *IEEE Access*, Vol. 8, 22 127–22 135, 2020.

[14] Samantaray, D., S. K. Ghosh, and S. Bhattacharyya, "Modified slotted patch antenna with metasurface as superstrate for dual-band applications," *IEEE Antennas and Wireless Propagation Letters*, Vol. 22, No. 1, 109–113, Jan. 2023.

[15] Qiu, L. and G. Xiao, "A broadband metasurface antenna array with ultrawideband RCS reduction," *IEEE Transactions on Antennas and Propagation*, Vol. 70, No. 9, 8620–8625, Sep. 2022.

[16] Nie, N.-S., X.-S. Yang, Z. N. Chen, and B.-Z. Wang, "A low-profile wideband hybrid metasurface antenna array for 5G and WiFi systems," *IEEE Transactions on Antennas and Propagation*, Vol. 68, No. 2, 665–671, Feb. 2020.

[17] Zhang, W., C. Song, R. Pei, Y. Huang, and J. Zhou, "Broadband metasurface antenna using hexagonal loop-shaped unit cells," *IEEE Access*, Vol. 8, 223 797–223 805, 2020.

[18] Kedze, K. E., H. Wang, and I. Park, "A metasurface-based wide-bandwidth and high-gain circularly polarized patch antenna," *IEEE Transactions on Antennas and Propagation*, Vol. 70, No. 1, 732–737, Jan. 2022.

[19] Nasser, S. S. S. and Z. N. Chen, "Low-profile broadband dual-polarization double-layer metasurface antenna for 2G/3G/LTE cellular base stations," *IEEE Transactions on Antennas and Propagation*, Vol. 70, No. 1, 75–83, Jan. 2022.

[20] Sultan, K. S., H. H. Abdullah, E. A. Abdallah, and H. S. El-Hennawy, "Metasurface-based dual polarized MIMO antenna for 5G smartphones using CMA," *IEEE Access*, Vol. 8, 37 250–37 264, 2020.

[21] Tariq, S., S. I. Naqvi, N. Hussain, and Y. Amin, "A metasurface-based MIMO antenna for 5G millimeter-wave applications," *IEEE Access*, Vol. 9, 51 805–51 817, 2021.

[22] Supreeyatitikul, N., A. Boonpoonga, and C. Phongcharoenpanich, "Z-shaped metasurface-based wideband circularly polarized Fabry–Pérot antenna for C-band satellite technology," *IEEE Access*, Vol. 10, 59 428–59 441, 2022.

[23] Melouki, N., A. Hocini, and T. A. Denidni, "High gain and wideband fabry-perot resonator antenna based on a compact single PRS layer," *IEEE Access*, Vol. 10, 96 526–96 537, 2022.

[24] Zawad, M., M. Z. M. Hamdalla, and A. M. Hassan, "Different geometrical representations of partially reflected surfaces for fabry-perot antenna optimization," in *2024 United States National Committee of URSI National Radio Science Meeting (USNC-URSI NRSM)*, 314–315, Boulder, CO, USA, Jan. 2024.

[25] Zawad, M., M. Z. M. Hamdalla, K. Durbhakula, and A. M. Hassan, "Performance comparison of different phase-gradient meta-surface unit cells for wide angle beam steering applications," in *2024 International Applied Computational Electromagnetics Society Symposium (ACES)*, 1–2, IEEE, 2024.

[26] Kolluru, C., M. Zawad, K. Durbhakula, T. Fields, A. M. Hassan, and M. Z. M. Hamdalla, "Design of a cavity-backed 360° beam steerable antenna for 5G wireless communication," in *2024 International Applied Computational Electromagnetics Society Symposium (ACES)*, 1–2, May 2024.

[27] Hamdan, S., E. K. I. Hamad, H. A. Mohamed, and S. A. Khaleel, "High-performance MTM inspired two-port MIMO antenna structure for 5G/IoT applications," *Journal of Electrical Engineering*, Vol. 75, No. 3, 214–223, Jun. 2024.

[28] Barad, D., J. C. Dash, D. Sarkar, and P. Srinivasulu, "Dual-band dual-polarized sub-6 GHz phased array antenna with suppressed higher order modes," *Scientific Reports*, Vol. 14, No. 1, 6139, Mar. 2024.

[29] Zhang, S., R. K. Arya, W. G. Whittow, D. Cadman, R. Mittra, and J. C. Vardaxoglou, "Ultra-wideband flat metamaterial GRIN lenses assisted with additive manufacturing technique," *IEEE Transactions on Antennas and Propagation*, Vol. 69, No. 7, 3788–3799, Jul. 2021.

[30] Chen, Z. N., T. Li, X. Qing, J. Shi, S. Li, Y. Su, W. E. I. Liu, C. Xue, Q. Lou, Z. H. Jiang, R. Xu, P. Liu, and H. Sheng, "Microwave metalens antennas," *Proceedings of the IEEE*, Vol. 111, No. 8, 978–1010, Aug. 2023.

[31] Kumari, N., M. Mahto, and P. K. Jain, "Cold-test characterization of metamaterial-assisted side coupled cavity," *IEEE Transactions on Electron Devices*, Vol. 70, No. 4, 1956–1961, Apr. 2023.

[32] Kumari, N., P. K. Jain, and M. Mahto, "Design study of a metamaterial-assisted reltron oscillator," *IEEE Transactions on Plasma Science*, Vol. 51, No. 8, 2212–2217, Aug. 2023.

[33] Zhang, X., S. Wang, J. Zou, H. Wang, J. Huang, Y. Li, Y. Liu, N. Li, H. Gong, Y. Gong, and Z. Duan, "Miniaturized P-band MW-level klystron with CeSRRs for CSNS linac application," *IEEE Transactions on Electron Devices*, Vol. 70, No. 9, 4878–4884, Sep. 2023.

[34] Thakur, A. S., M. Rawat, and M. V. Kartikeyan, "Design of an oppositely-oriented circular split-ring resonator-loaded multibeam all-metallic metamaterial backward-wave oscillator," *IEEE Transactions on Plasma Science*, Vol. 51, No. 9, 2625–2631, Sep. 2023.

[35] Hamdalla, M. Z. M., R. Allen, P. J. Bland, and A. M. Hassan, "Cavity backed metasurface antenna for high power applications," in *2023 IEEE International Symposium on Antennas and Propagation and USNC-URSI Radio Science Meeting (USNC-URSI)*, 1085–1086, Portland, OR, USA, Jul. 2023.

[36] Chen, R.-S., L. Zhu, J.-Y. Lin, S.-W. Wong, Y. Yang, Y. Li, L. Zhang, and Y. He, "High-efficiency and wideband dual-resonance full-metal cavity-backed slot antenna array," *IEEE Antennas and Wireless Propagation Letters*, Vol. 19, No. 8, 1360–1364, Aug. 2020.

[37] Carvalho, S. S., J. R. V. Reis, A. Mateus, and R. F. S. Caldeirinha, "Exploring design approaches for 3D printed antennas," *IEEE Access*, Vol. 12, 10 718–10 735, 2024.

[38] Zheng, Y., M. Gao, and X. Zhao, "A broadband multimode antenna with enhanced gain and high efficiency by employing metasurface for WLAN and car-to-car application," *IEEE Access*, Vol. 10, 90 647–90 654, 2022.

[39] krn5, "CST Studio Suite 3D EM simulation and analysis software," [Online]. Available: https://www.3ds.com/products-

services/simulia/products/cst-studiosuite/, Oct. 2023.

[40] Pozar, D. M., *Microwave Engineering: Theory and Techniques*, John Wiley & Sons, 2021.

[41] Kedze, K. E., H. Wang, Y. B. Park, and I. Park, "Substrate dielectric constant effects on the performances of a metasurface-based circularly polarized microstrip patch antenna," *International Journal of Antennas and Propagation*, Vol. 2022, No. 1, 3026677, Sep. 2022.

[42] Hamdalla, M. Z. M., A. N. Caruso, and A. M. Hassan, "Electromagnetic compatibility analysis of quadcopter UAVs using the equivalent circuit approach," *IEEE Open Journal of Antennas and Propagation*, Vol. 3, 1090–1101, 2022.

[43] Quintero, G., J.-F. Zurcher, and A. K. Skrivervik, "System fidelity factor: A new method for comparing UWB antennas," *IEEE Transactions on Antennas and Propagation*, Vol. 59, No. 7, 2502–2512, Jul. 2011.

[44] De León, G. Q. D., "Analysis and design of ultra-wideband antennas in the spectral and temporal domains," *Ecole Polytechnique Fédérale de Lausanne*, 2010.

[45] Anza, S., C. Vicente, J. Gil, M. Mattes, D. Wolk, U. Wochner, V. E. Boria, B. Gimeno, and D. Raboso, "Prediction of multipactor breakdown for multicarrier applications: The quasi-stationary method," *IEEE Transactions on Microwave Theory and Techniques*, Vol. 60, No. 7, 2093–2105, Jul. 2012.

[46] Chen, R.-S., S.-W. Wong, G.-L. Huang, Y. He, and L. Zhu, "Bandwidth-enhanced high-gain full-metal filtering slot antenna array using TE_{101} and TE_{301} cavity modes," *IEEE Antennas and Wireless Propagation Letters*, Vol. 20, No. 10, 1943–1947, Oct. 2021.

[47] Goudarzi, A., M. M. Honari, and R. Mirzavand, "A high-gain leaky-wave antenna using resonant cavity structure with unidirectional frequency scanning capability for 5G applications," *IEEE Access*, Vol. 9, 138 858–138 865, 2021.

[48] Guan, Y., Y.-C. Jiao, Y.-D. Yan, Y. Feng, Z. Weng, and J. Tian, "Wideband and compact Fabry–Perot resonator antenna using partially reflective surfaces with regular hexagonal unit," *IEEE Antennas and Wireless Propagation Letters*, Vol. 20, No. 6, 1048–1052, Jun. 2021.

[49] Chen, R.-S., L. Zhu, S.-W. Wong, J.-Y. Lin, Y. Li, L. Zhang, and Y. He, "S-band full-metal circularly polarized cavity-backed slot antenna with wide bandwidth and wide beamwidth," *IEEE Transactions on Antennas and Propagation*, Vol. 69, No. 9, 5963–5968, Sep. 2021.